

# Application of Envelope-following Techniques to the Simulation of Hybrid Power Systems

D. Linaro *Member, IEEE*, D. del Giudice *IEEE Student Member*, A. Brambilla *Member, IEEE*, F. Bizzarri, *Senior Member, IEEE*

**Abstract**—The dynamics of modern hybrid power systems are characterized by behaviors at different timescales, typically separated by several orders of magnitude. In this paper we apply the envelope-following method to hybrid power systems simulations, in which single-phase and three-phase representations of a power system co-occur. This simulation method is well suited for handling coexisting behaviors occurring at different timescales. Compared to the simulation approaches present in the literature, the envelope-following method does not need to continuously switch between two separate simulation engines, but rather automatically handles instantaneous variations in the dynamics of the system, such as faults or topology changes. Additionally, given the vast penetration of power electronic components in modern electricity networks, employing the envelope-following method allows using a vast array of numerical algorithms that have been developed over the years to simulate electrical and electronic circuits. The proposed approach is validated by means of power systems case studies of increasing complexity.

**Index Terms**—Power system, envelope following method, time domain circuit simulation, photovoltaic system simulation, hybrid power system.

## I. INTRODUCTION

IN the last decades an increasing number of distributed energy resources and non-conventional loads have been installed in distribution systems and portions of the same transmission system. Separate transmission systems have been interconnected by high-voltage direct current (HVDC) and multi-terminal direct current (MTDC) systems. In the literature, these mixed systems are referred to as *hybrid power systems* [1]. The electrical characteristics of these systems have changed the simulation paradigm and led to the need of simultaneously simulating the power generation and transmission systems together with the power distribution systems, at the cost of higher simulation time and complexity. Before the arrival of hybrid power systems, in general electromagnetic transient (EMT) simulation tools were not used in the analysis of conventional generation and transmission systems because of their heavy computational load. Single-phase equivalent models and *ad hoc* simulation tools were and are usually employed to accelerate the simulations. The large penetration

of electronically connected loads and local generations by renewable sources requires simulating distribution systems with EMT simulation tools adopting accurate three-phase models, which has thus an impact on the overall simulation efficiency.

This has led to the introduction of the concept of *hybrid simulation*, in which single-phase and three-phase representations of a power system coexist in the same simulation [2]–[5]. For example, [2], [3] proposed a robust and flexible simulation scheme that switches from hybrid simulation mode back to pure phasor-domain dynamic simulation mode to achieve significantly improved simulation efficiency. Another instance of the application of the hybrid simulation paradigm is [6], where the authors proposed a benchmark transmission and distribution system, and showed that the total computational time was significantly reduced compared to running the EMT hybrid simulation for the whole simulation period, while maintaining good simulation accuracy. Additional hybrid simulation approaches can be found in [7] and [8]: the former describes an EMT/electromechanical hybrid simulator suited to modern HVAC and DC power systems, while the latter introduces a simulation tool used to study the impact of integration of photovoltaic systems on distribution networks. We refer the interested reader to [9]–[12] for additional approaches to the hybrid simulation of power systems.

Albeit successful, the hybrid approach to the simulation of power systems dynamics is characterized by several critical aspects. First of all, the presence of two simulators running in parallel creates the need for complex “synchronization” strategies. In [2], [3], for instance, the transient stability (TS) simulation is always running, even when the EMT simulation is “in control”. An even more problematic aspect of having two simulators is that the switch from EMT to TS simulation happens when the two concurrent solutions converge to an “identical” one. This implies that the results of the two representations must tend to the same solution, which may not be the case, due for example to different models of parts of the entire power system [3].

Here, we propose a novel approach to the simulation of power system dynamics that mitigates the long-standing problems related to the usage of EMTP-like simulators, while at the same time not requiring to continuously switch between two separate simulation engines. The key point consists in employing a single simulation engine capable of dealing with both a single-phase equivalent and a full three-phase model. The former can embody a portion of the generation and transmission sub-system, generally characterized by electromechanical models with relatively slow dynamics. On the contrary,

Angelo Brambilla, Davide del Giudice and Daniele Linaro are with Politecnico di Milano, DEIB, Piazza Leonardo da Vinci, 32, I-20133 Milano, Italy. (e-mail: {angelo.brambilla, danielle.linaro, davide.delgiudice}@polimi.it). Federico Bizzarri is with Politecnico di Milano, DEIB, Piazza Leonardo da Vinci, 32, I-20133 Milano, Italy and also with the Advanced Research Center on Electronic Systems for Information and Communication Technologies E. De Castro (ARCES), University of Bologna, 41026 Bologna, Italy. (e-mail: federico.bizzarri@polimi.it).

the latter incorporates the remaining parts of the network (distribution system included) contributing fast dynamics. In addition, as highlighted in the following, the components of the three-phase subsystem (e.g., distribution feeders, circuit breakers, AC/DC systems, and converters) potentially feature a high degree of detail.

Importantly, it is up to the users to decide how to partition the full power system, based on details that are needed in simulating the entire hybrid system. However note that partitioning must be also driven by the characteristics of the used models. The single-phase one may account for both the positive and negative sequence components (albeit being extremely efficient when only the former is present), but it disregards zero sequence components that may arise during unbalanced operating conditions (e.g., single line-to-ground faults). To address this issue, the zero sequence must be confined in the detailed three-phase model. This can be easily accomplished by exploiting  $YY_g$  or  $\Delta Y_g$  transformers as possible boundary elements between two sub-systems modeled with a single and three-phase model, respectively. Indeed, these transformers prevent zero sequence currents from flowing from their secondary to primary windings.

The envelope-following method (EFM) we propose builds on previous works [13], [14], in which we showed how to efficiently interface the single-phase and three-phase portions of the full system and how to initialize them. Here, we describe how to perform simulations either with a conventional transient analysis or with the EFM [15]–[19], which, as we will see, greatly reduces the time to solution. The motivation behind the usage of EFMs lays in the fact that in the simulation of hybrid power systems, where some parts are described by detailed three-phase models, the integration time step must be much smaller than the system frequency (i.e.,  $1/T = 50$  Hz or 60 Hz) to achieve an adequate degree of accuracy. In most cases of practical importance, this constraint constitutes a “best-case scenario”. Indeed, if the three-phase system under analysis contains for instance power converters described by detailed switching models, the integration time step must be at least comparable to the internal clock signals, i.e., it can drop to a few tens of micro-seconds, while the time intervals of interest may be in the order of thousands or even tens of thousands of periods  $T$ . Additionally, one is typically not interested in the details of voltages or currents during every period  $T$ , but rather in the long-term dynamics of other network quantities, such as the generators’ angular frequency. We show that EFM allows performing simulations spanning thousands of periods in a relatively short CPU time, with only a minor sacrifice in terms of accuracy, by integrating only a reduced number of periods and then doing a forward computation of the solution.

The paper is organized as follows: in Sec. II we describe the mathematical foundations of the extension of the EFM to hybrid power systems and in Sec. III we provide some details about the EFM. In Sec. IV we present three test cases to highlight the main features of the proposed approach and finally in Sec. V we discuss the main results of our work.

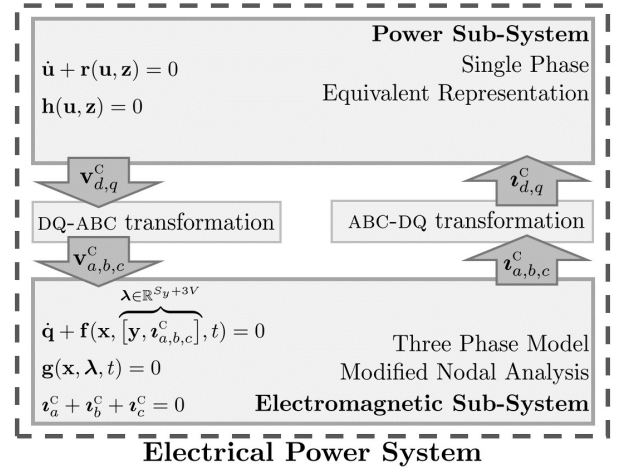


Figure 1. High-level block schematic of an electrical power system. The classical power system model (PSM) of the PSS and the MNA three-phase model of the ESS communicate at  $V$  connection points through as many *connectors*.

## II. ELECTRICAL POWER SYSTEM MODELING

Figure 1 shows a high-level block schematic of an electrical power system. It represents an electrical network split into two distinct parts, the power electromechanical sub-system (PSS) model and the electromagnetic sub-system (ESS) model. The former and latter are described by the classical power system model (PSM) [20] (i.e., by the single-phase equivalent model) and a three-phase EMT dynamic model, respectively. The entire power system exploits the modified nodal analysis (MNA) representation to implement the constitutive equations of elements [21], [22]. To enable the *communication* between these two sub-systems,  $V$  connection points, corresponding to as many *virtual connectors*, are added. These elements are not present in the original description of the system: rather, they are introduced by the user as interfacing elements between the two simulation models.

The set of differential algebraic equations (DAEs) ruling the dynamics of the overall electrical power system is [23]

$$\dot{\mathbf{u}} + \mathbf{r}(\mathbf{u}, \mathbf{z}) = 0, \quad \mathbf{h}(\mathbf{u}, \mathbf{z}) = 0, \quad (1a,b)$$

$$\dot{\mathbf{q}}(\mathbf{x}) + \mathbf{f}(\mathbf{x}, \underbrace{[\mathbf{y}, \mathbf{v}_{a,b,c}^c]}_{\lambda \in \mathbb{R}^{S_y+3V}}, t) = 0, \quad \mathbf{g}(\mathbf{x}, \lambda, t) = 0, \quad (1c,d)$$

$$\mathbf{v}_a^c + \mathbf{v}_b^c + \mathbf{v}_c^c = 0. \quad (1e)$$

Equations 1a and 1b refer to the power electromechanical sub-system (PSS) model:  $\mathbf{u} \in \mathbb{R}^{S_u}$  are the state variables (introduced for example by generators, regulators, controllers) spanning the PSS phase space and  $\mathbf{z} \in \mathbb{R}^{S_z}$  are the algebraic variables (e.g. bus voltages, currents). Equations 1c and 1d refer to the electromagnetic sub-system (ESS):  $\mathbf{x} \in \mathbb{R}^{S_x}$  are the state variables (i.e., capacitive voltages and inductive currents),  $\mathbf{y} \in \mathbb{R}^{S_y}$  are the algebraic variables (i.e., ground-referenced node voltages and branch currents), and the entries of  $\mathbf{q} : \mathbb{R}^{S_x} \rightarrow \mathbb{R}^{S_x}$  are capacitive charges and inductive fluxes. The  $V$  pairs of voltages  $\mathbf{v}_{d,q}^c = [v_{d,q}^{c1}, \dots, v_{d,q}^{cV}]$  at the corresponding connection buses, where virtual connectors

are inserted, feed the ESS through  $V$  triplets of voltages  $\mathbf{v}_{a,b,c}^c = [v_{a,b,c}^{c_1}, \dots, v_{a,b,c}^{c_V}]$  set by  $V$  three-phase controlled voltage sources, which are obtained by applying the DQ-ABC transformation to  $\mathbf{v}_{d,q}^c$ . These circuit elements do not admit voltage basis and consequently since we use MNA, the algebraic-variable vector is enlarged with the  $V$  triplets of currents  $\mathbf{i}_{a,b,c}^c = [i_{a,b,c}^{c_1}, \dots, i_{a,b,c}^{c_V}]$  flowing through them (see the  $\boldsymbol{\lambda}$  vector in Eqs. 1c and 1d). The  $\mathbf{i}_{d,q}^c$  currents at the PSS side are obtained from the  $\mathbf{i}_{a,b,c}^c$  currents at the ESS through the ABC-DQ transformation. Equation 1e implements a constraint that forces to zero the 0 component of the  $\mathbf{i}_{a,b,c}^c$  currents. This is done to ensure that these components are not injected in the PSS, since the PSM of the PSS is developed by assuming that 0 components are null. This assumption replicates what happens in practice when  $\Delta Y_g$  or  $YY_g$  transformers are used in feeders.

The DAEs in Eqs. 1 are recast gathering the differential equations and the algebraic constraints, thus obtaining the following semi-explicit index-1 DAE [24] and initial conditions

$$\dot{\boldsymbol{\xi}} = \boldsymbol{\gamma}(\boldsymbol{\xi}, \boldsymbol{\psi}, t), \quad \boldsymbol{\eta}(\boldsymbol{\xi}, \boldsymbol{\psi}, t) = 0, \quad (2a,b)$$

$$\boldsymbol{\xi}(t_0) = \boldsymbol{\xi}_0, \quad \boldsymbol{\eta}(\boldsymbol{\xi}_0, \boldsymbol{\psi}_0, t_0) = 0, \quad (2c,d)$$

where  $\boldsymbol{\xi} = [\mathbf{u}, \mathbf{x}] \in \mathbb{R}^{S_u+S_x}$ ,  $\boldsymbol{\psi} = [\mathbf{z}, \boldsymbol{\lambda}] \in \mathbb{R}^{S_z+S_y+3V}$ , and

$$\begin{aligned} \boldsymbol{\gamma} : \mathbb{R}^{S_u+S_x+S_z+S_y+3V+1} &\rightarrow \mathbb{R}^{S_u+S_x} \\ \boldsymbol{\eta} : \mathbb{R}^{S_u+S_x+S_z+S_y+3V+1} &\rightarrow \mathbb{R}^{S_z+S_y+3V} \end{aligned}$$

The steady-state solution of power systems such as those in Fig. 1 and described using this mathematical formalism is not constant but oscillates at least in the three-phase model and it may do so in the single-phase model as well if there are negative components or harmonics [14]. It reduces to the well-known power flow (PF) solution when the ESS is not present. To compute the steady-state solution one has to resort to methods such as the one presented in detail in [13], which we employed in all the examples described in the following (but see [25], [26] for possible alternative methods).

In Appendix we consider a basic version of an AC/DC system, whose purpose is twofold: first, by means of pen-and-paper calculations, it shows how the general structure of Eq. 2 can be derived. Secondly, it further proves that the EFM can be effectively used to simulate AC/DC systems (this latter aspect is also shown by the third case study in Sec. IV-D).

### III. THE ENVELOPE-FOLLOWING METHOD

The envelope-following method (EFM) [18], [19] is an algorithm that finds widespread application in the computation of the numerical solution of a system of DAEs that display oscillatory behavior [15], [17], [27]–[30], with a high-frequency component of period  $T$ , which is either constant or slowly varying with time. In these systems, it is thus possible to reduce the simulation time without compromising accuracy by exploiting the fact that the behavior of such a system in a given period  $T$  is similar, but not identical, to its behavior in the preceding and following ones. At its core, the algorithm consists in using the information obtained by conventionally solving the system of DAEs over a single period

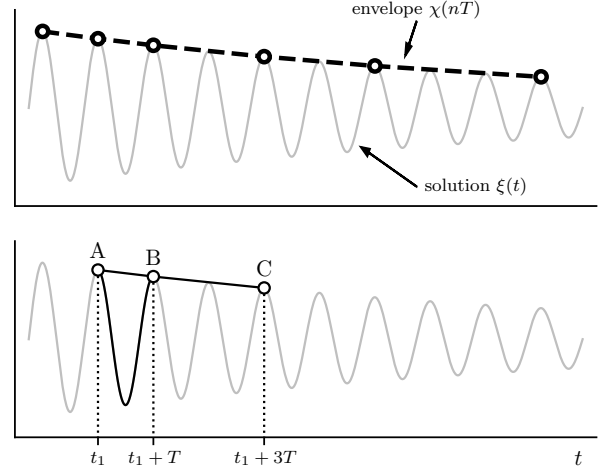


Figure 2. Example of the envelope-following method: the gray continuous trace is the conventional solution  $\boldsymbol{\xi}(t)$  of Eq. 2, while the black circular markers indicate the  $\boldsymbol{\chi}$  samples that make up the envelope of the solution. The bottom panel shows how the solution over one period (black trace from points A to B) is used to project the envelope solution two periods ahead in time to point C.

to accurately “project” the solution several periods (possibly hundreds) ahead in time (see Fig. 2 for an example), thus substantially speeding-up the computation of the solution over very long time intervals. The  $\boldsymbol{\chi}$  sequence formed by sampling the  $\boldsymbol{\xi}(t)$  state vector (black circular markers in Fig. 2, see Eq. 2), i.e.,  $\boldsymbol{\chi} = \{\boldsymbol{\xi}(t_1+T), \boldsymbol{\xi}(t_1+2T), \dots, \boldsymbol{\xi}(t_1+mT)\}$ , must change slowly as a function of  $m$  ( $t_1 \geq t_0$ ). The continuous function obtained by interpolating  $\boldsymbol{\chi}$  for  $t \in [t_1+T, t_1+mT]$  is defined as the *envelope solution* of Eq. 2 (dashed black line in Fig. 2). To derive a “differential-like” evolution law for the elements of  $\boldsymbol{\chi}$ , the *envelope vector field* is introduced

$$\boldsymbol{\rho}(t_1, \boldsymbol{\xi}(t_1), \boldsymbol{\xi}(t_1+T)) = \frac{1}{T}(\boldsymbol{\xi}(t_1+T) - \boldsymbol{\xi}(t_1)), \quad (3)$$

where system (2) is integrated from  $t_1$  to  $t_1+T$  with conventional methods (black continuous line in the bottom panel of Fig. 2). If one is interested in computing  $\boldsymbol{\xi}(t_1+mT)$  from  $\boldsymbol{\xi}(t_1+nT)$  ( $m-n \geq 1$ ) it is possible to write

$$\begin{aligned} \boldsymbol{\xi}(t_1+mT) &= \boldsymbol{\xi}(t_1+nT) + \\ &+ H\boldsymbol{\rho}(t_1+nT, \boldsymbol{\xi}(t_1+nT), \boldsymbol{\xi}(t_1+(n+1)T)), \end{aligned} \quad (4)$$

where  $H = (m-n)T$  is the *forward envelope time step*: in the example shown in Fig. 2,  $n=0$  and  $m=3$ . This corresponds to adopting the explicit Euler integration method to predict the next value of the envelope. In (4)  $\boldsymbol{\xi}(t_1+nT)$  is known,  $\boldsymbol{\xi}(t_1+mT)$  is the unknown envelope solution at  $m-n$  times the period  $T$  after  $t_1+nT$ , where the envelope solution is known. The envelope vector field is obtained by integrating the envelope solution from  $t_1+nT$  to  $t_1+(n+1)T$ , i.e., along one period  $T$  from  $t_1+nT$ . To this end we used either the trapezoidal method or the Gear method up to order 6 [31]. In the latter case we adapted the order by varying it along the  $[t_1+nT, t_1+(n+1)T]$  integration time interval. We used a variable time step, as a large number of simulators do, to meet

accuracy and numerical efficiency. So doing, the computation of the solution of the complete system along  $m - n$  periods  $T$  is skipped. This is not the only possible strategy, i.e., one can resort, for instance, to the implicit Euler integration method

$$\begin{aligned} \xi(t_1 + mT) &= \xi(t_1 + nT) + \\ &+ H\rho(t_1 + mT, \xi(t_1 + mT), \xi(t_1 + (m + 1)T)) , \end{aligned} \quad (5)$$

or the trapezoidal rule

$$\begin{aligned} \xi(t_1 + mT) &= \xi(t_1 + nT) + \\ &+ \frac{H}{2} [\rho(t_1 + nT, \xi(t_1 + nT), \xi(t_1 + (n + 1)T)) . \end{aligned} \quad (6)$$

Equations 5 and 6 represent the corrector step of a predictor-corrector algorithm, where the predictor part is given by Eq. 4. The associated local truncation errors (LTEs) for the implicit Euler method (IE) and trapezoidal rule (TR) are respectively  $\mathcal{O}(H^2)$  and  $\mathcal{O}(H^3)$ , and are given by

$$\begin{aligned} \text{LTE}_{\text{IE}} &= \frac{H^2}{2} \ddot{\xi}(t) \\ \text{LTE}_{\text{TR}} &= \frac{H^3}{12} \ddot{\xi}(t) . \end{aligned} \quad (7)$$

By defining an appropriate limit on the LTE of the envelope solution, one can therefore implement an adaptive procedure to adjust the envelope time step  $H$  to meet the required accuracy level.

Additionally, whenever  $\xi(t)$  starts displaying fast transient variations with respect to  $T$ , it will not be possible for the EFM to maintain the error below a suitable threshold value and therefore the envelope integration time step will be progressively reduced until it reaches the minimum value of  $H = 1$ , which corresponds to a conventional integration of Eq. 2. Further details on the EFM can be found in [17]. We point out that in the examples described in this paper, the period  $T$  is constant and known to the simulator. However, our simulator PAN can also deal with systems in which  $T$  varies slowly with time: in such cases, the time-varying value of  $T$  is detected by determining the instants at which a subset of the state variables crosses an appropriate Poincaré section.

The solution obtained with the EFM consists of a set of points that lie on the envelope of the full solution (black circular markers and gray trace in Fig. 2, respectively). Importantly, each envelope point can be used as a starting point for a conventional integration algorithm, if a more detailed solution is required at specific points in time. As a matter of fact, each envelope point belongs to a *ball*, which is centered at a point of the overall conventional solution, whose radius depends on the chosen envelope tolerances. As a consequence, as the envelope algorithm actually does, each point of the envelope solution can be profitably used to start a conventional integration solution whenever needed/desired.

#### IV. HYBRID POWER SYSTEM SIMULATION

In this section we apply the proposed envelope-following method (EFM) to power systems described by coexisting single-phase (power electromechanical sub-system (PSS)) and

three-phase (electromagnetic sub-system (ESS)) models, characterized by widely separated time constants. We present three test cases of increasing complexity to validate the proposed EFM (an additional simple test case is reported in the Appendix). The simulation results were obtained with our simulator PAN [32], [33], in which we implemented the EFM.<sup>1</sup> While we make direct comparisons with the conventional, variable time step transient analysis available in PAN, we chose not to use other simulators for the difficulty in obtaining either their source code or a usable copy.

##### A. Model of a distribution feeder

Following what was done in [2], we modeled the distribution systems by means of the 8-bus distribution feeder shown in Fig. 3. The feeder is made up of eight buses connected by non-perfectly transposed overhead lines, whose parameters and line codes are taken from the IEEE 13-bus test feeder [34], [35]. As shown in Fig. 3, a total of seven balanced and wye-connected resistive loads, adding up to 8 MW at a nominal bus voltage of 12.47 kV, are connected to the distribution feeder. Additionally, three capacitive loads totaling 1.2 MVAR are connected to buses 3, 5 and 7. Throughout this paper, the distribution feeder and the parts of the networks connected to it are modeled with a detailed three-phase representation (necessary for the single phase-to-ground fault simulations described in the following).

##### B. Hybrid system 1

The first test case we consider is shown in Fig. 4: it consists of a three-phase generator (whose model includes a turbine governor and an automatic voltage regulator) connected by means of a three-phase line to a balanced 100 MW load and to the previously described distribution feeder. We applied a single line-to-ground fault at phase A of bus 7 of the feeder lasting 5 periods of the 60 Hz nominal system frequency, and recorded the three-phase voltages at buses 2 and 7 of the feeder and bus 3 outside of the feeder. Note that the  $YY_g$  and  $\Delta Y_g$  transformers prevent the propagation of the zero sequence to the single phase model, but do not eliminate the presence of the negative sequence and harmonics.

Figure 5 shows the results of this simulation: the black dots in the panels on the left correspond to the maxima of the fast oscillations in each period. As can be seen, the application of the fault at bus 7 of the feeder causes a marked decrease in the voltage of phase A of all the buses of the system, with a magnitude that depends on the distance between the bus where the measurement is made and the fault location.

Interestingly, as shown in Fig. 5, the bus voltages return to their pre-fault values in approximately 5 s. However, due to the internal dynamics of the three-phase generator, the timescale of the dynamics of the angular frequency of the machine following the application of the fault is markedly slower as shown in Fig. 6. The fault causes a deviation in the rotation speed of approximately 0.5 mpu in the first few

<sup>1</sup>The files necessary to simulate with PAN the case studies presented in this section are available on GitHub at the address <https://github.com/danielelinaro/power-envelope-paper.git>.

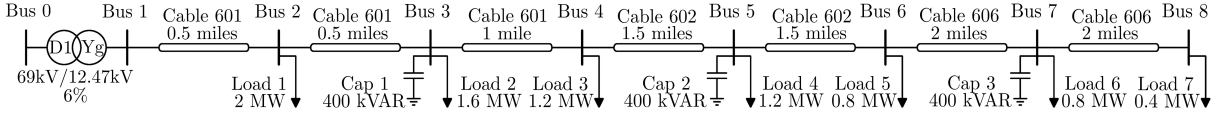


Figure 3. Model of the distribution feeder used in this study.

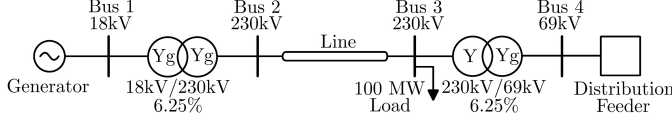


Figure 4. Generator with feeder: the three-phase generator is characterized by internal dynamics and contains a turbine governor and an automatic voltage regulator. The part of the system to the left of bus 3 is described by a single-phase representation, while the rest of the system is modeled with a detailed three-phase representation.

seconds immediately after the fault; at the same time, the generator speed returns to its operating point value over a time interval that is markedly different from what we showed for the electrical quantities of the system, since it happens over a time course of hundreds of seconds.

As mentioned in the Introduction, one is typically interested in simulating the detailed dynamics of bus voltages and currents from just before the application of the fault to right after its clearing, but is not interested in a detailed simulation (i.e., very short integration time step) after the fault clearing. On the other hand, there is interest in having an idea of the timescale over which the generators in the network return to their normal operating point following a disturbance. As a consequence, the application of EFM is perfectly suited to achieving this goal. Figure 5 shows the results of simulating the system in Fig. 4 during the application of a single line-to-ground fault on bus 7 of the feeder. The procedure employed to obtain the solution fundamentally differs from that used with conventional integration methods: gray dots were obtained *after* the simulation, by extracting the peaks of each period, while the black circular markers are the *actual points* of the envelope solution computed by the algorithm. Notice that the scale of the panels on the right side is such that the gray dots appear as a continuous line. This allows one to appreciate the substantial reduction in terms of complexity of the solution achievable by using EFMs. Additionally, we remark that each point of the envelope solution can be used as a starting point for a detailed integration, should one be interested in obtaining additional details on a specific time interval.

The bottom panel of Fig. 6 shows the length  $H$  of the time steps taken by the EFM. A value of 50, for instance, means that the algorithm places one point every 50 periods of the full solution of the system, obtained by conventional methods. It is worth noticing that the  $H$  time step automatically reduces at the time instant of occurrence of the fault and later increases again until  $H = 300$  once the fault has been cleared. This adjustment mechanism grants the EFM a substantial speed-up [18], [19]. To validate this statement, we compared the CPU time needed by the conventional transient

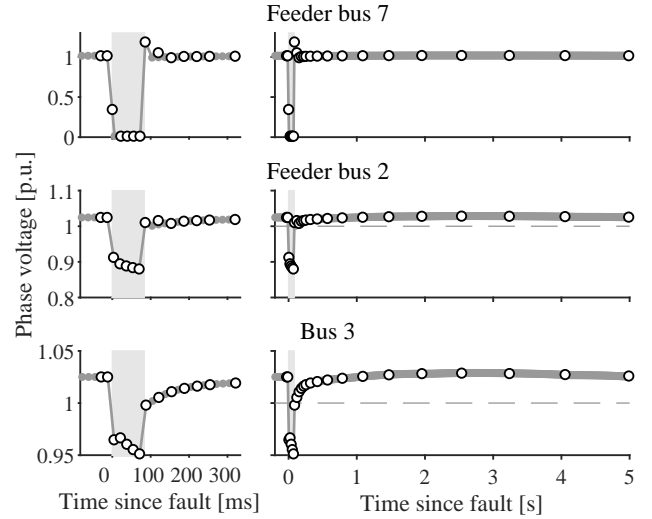


Figure 5. Phase A voltages at buses 7 and 2 inside the distribution feeder and at bus 3 outside the distribution feeder following the application of a single line-to-ground fault at bus 7 (phase A) of the feeder. Notice how the voltages return to their pre-fault values in approximately 5 s. Black circles represent the solution obtained by the envelope-following algorithm, while gray dots are the maxima, in each period, of the solution obtained with a conventional variable time-step integration method (i.e., they represent the “true” envelope of the solution). The scale of the right-hand panels is such that the gray dots appear as an uninterrupted line. The light gray patches indicate the time interval where the fault was applied.

analysis with a *variable* time step and with the envelope-following algorithm to obtain the results shown in Figs. 5 and 6. The former and latter respectively required 379 s and 15 s to simulate 400 s of network time on the same computer and with the same software environment, which corresponds to a  $25\times$  speed-up. Note that this result has been achieved without sacrificing accuracy: indeed, the root mean squared error (RMSE) between the two solutions remains always well within acceptable values, as shown in Table I for the electrical variables shown in Fig. 5. The calculation of the RMSE was subdivided before and after the fault due to the change in range (i.e., the difference between maximum and minimum values) of several electrical quantities, which would have otherwise resulted in an incorrect quantification of the error either before or after the fault for those variables.

We remark here that the usage of either integration techniques, i.e., conventional transient integration or EFM, does not require any specific strategy to deal with discontinuities such as those introduced by faults in the system. This is a marked paradigm shift in comparison to the simulation approaches described in [2], [3] and mentioned in the Introduction, which rely on two simulators running in parallel and on a heuristic to appropriately switch between simulators.

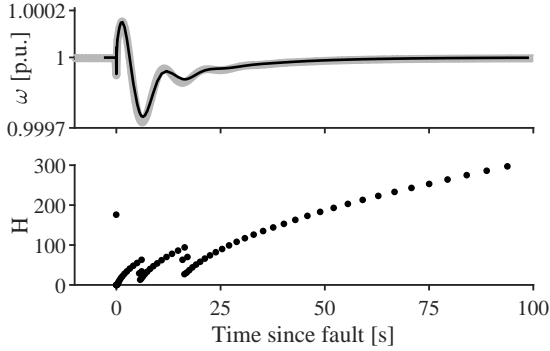


Figure 6. Top panel: angular frequency  $\omega$  of the generator (gray and black traces obtained with conventional and envelope-following algorithms, respectively). Bottom panel: envelope time step, in units of periods of the underlying oscillation at 60 Hz.

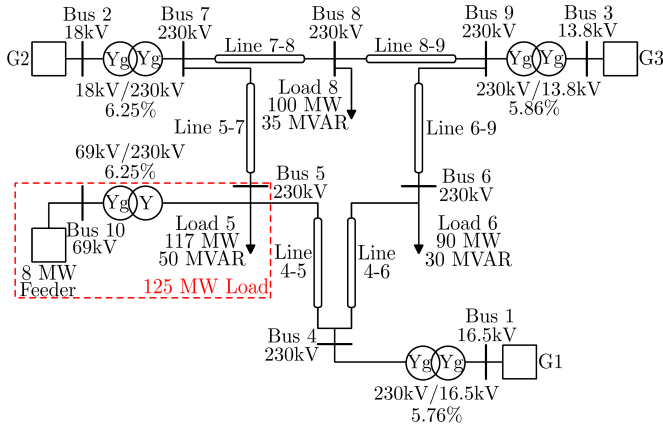


Figure 7. Schematic of the 9-bus, 3-generator WSCC system. The distribution feeder connected to bus 10 is modeled with a detailed three-phase representation. The rest of the power system is described by a single-phase model.

### C. The WSCC 9-bus system

The second example we considered is the WSCC 9-bus system in Fig. 7. It implements an extremely simplified version of the Western System Coordinating Council network [36] and is widely used in the literature as a test case [37]–[39]. We substituted part of the original 125 MW load connected to bus 5 with the distribution feeder we used throughout this work, as shown in Fig. 7.

To investigate the applicability of EFMs to this test case, we applied once again a single line-to-ground fault at phase A of bus 7 of the feeder. In this instance, however, we included

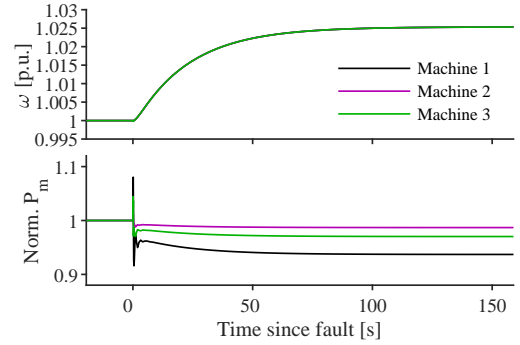


Figure 8. Dynamics of the angular frequency (top panel) and mechanical power (bottom panel) of the generators of the 9-bus WSCC network in response to the application of a single line-to-ground fault. See Fig. 9 for a zoom of the time interval surrounding the application of the fault.

in the distribution feeder a sulfur hexafluoride (SF6) circuit breaker [40]–[42], whose detailed model takes into account the fast dynamical behavior (in the range of the  $\mu$ s) of the plasma [43]. The SF6 breaker is connected between the D1Yg transformer and bus 1 of the feeder shown in Fig. 3. Its purpose is to disconnect the distribution feeder 200 ms after the occurrence of the fault.

To show the potentiality of the proposed envelope following method, our target is to accurately simulate both the very short-term behavior ( $\mu$ s) of the SF6 breaker that isolates the feeder and the long-term behavior on the WSCC system after the feeder is disconnected. The disconnection of the feeder causes an overall decrease of the load connected to the WSCC network<sup>2</sup>. As shown in Fig. 8, this results in an increase in the rotor frequency  $\omega$  of the three machines (top panel) and in a corresponding decrease of their mechanical input power given by turbine governors (bottom panel), which takes place right after the “spike” caused by the fault.

The variation in generator angular frequency and mechanical power happens over timescales of the order of the hundreds of seconds: this, combined with the fact that the detailed model of the SF6 breaker we employed adds significant numerical complexity to the simulation and that the arcs quench in a time interval smaller than some tens of  $\mu$ s, implies that conventional approaches to the simulation of this type of systems, over the time course shown here, would require a prohibitively large amount of time to provide a solution. For example, if a *fixed* time step of 1  $\mu$ s were used to accurately simulate the dynamics of the arcs and we were interested in the behavior of the WSCC system after the feeder disconnection (lasting about 150 s) an EMT-like simulation would have to compute 150,000,000 time points. Also in this case we compared the conventional transient analysis with a *variable* time step and the envelope-following algorithm in terms of simulation time, obtaining a speed-up of approximately 17 $\times$  (3058 s and 182 s for the former and latter analyses, respectively, to simulate 400 s of network time). Beyond the significant speed-up in terms of simulation time, the approach outlined here with

<sup>2</sup>The total decrease of the mechanical power of the three machines amounts to 7.6 MW, which is in line with the nominal power absorbed by the loads connected to the distribution feeder.

Table I  
RMSE BETWEEN CONVENTIONAL EMT INTEGRATION AND EFM FOR THE TRACES SHOWN IN FIG. 5

Variable	Before fault		After fault	
	RMSE	Range	RMSE	Range
Feeder bus 7 voltage	4.2 V	35.8 kV	103 V	86.3 kV
Feeder bus 2 voltage	4.2 V	36.1 kV	22 V	36.3 kV
Bus 3 voltage	77 V	667 kV	79 V	669 kV

a single simulation engine allows one to include accurate models of various parts of the system, similarly to what we did for the circuit breaker. To highlight this key feature, we analyzed in more detail the dynamics of the system around the time of the application of the fault. The results are shown in Fig. 9: as it can be seen from panel E, by looking at currents across the SF6 breaker one can easily discern both the instant of the application of the fault (at  $t = 0$  ms) and that of the opening of the breaker (at  $t = 200$  ms). Panels C and D show respectively the dynamics of the machines' angular frequency and mechanical power. The former displays oscillatory behavior between the onset of the fault and the opening of the breaker due to the presence of relevant negative sequence components. Finally, panels E and F present the behavior of some of the electrical quantities associated with the three-phase circuit breaker, namely the arc currents and voltages: the former shows a clear increase in the phase A current following the fault until the opening of the breaker, while the latter are non-zero only after the opening of the breaker. These waveforms show constant parts although they oscillate at (about) 60 Hz because the points that are  $H$  periods apart in the envelope solution are connected in the figure.

To better characterize the ability of the EFM to adapt the integration of the envelope portion of the solution, we report in panels G and H the current of phase A of the SF6 breaker during zero crossing when the arc quenches and the corresponding voltage across the breaker (transient recovery voltage). The tail current (due to charge recombination in the quenching arc) beginning just after voltage zero crossing reaches a negative peak of a few amperes due to the negative transient recovery voltage across the arc: in this current interruption, the recovery voltage does not pose any problem. The interrupted currents of phases B and C, while behaving in a qualitatively similar way, are significantly smaller in magnitude than the current of phase A.

The RMSE between conventional and EFM solutions is well within acceptable values, as indicated in Table II for all the electrical variables shown in Fig. 9. In the table, N/A indicates that the range of a given variable before or after the fault was below the numerical absolute tolerance of the integration method.

These results highlight the flexibility of the proposed method: employing EFM grants a substantial reduction in the time to solution, with only minor sacrifices in terms of accuracy of

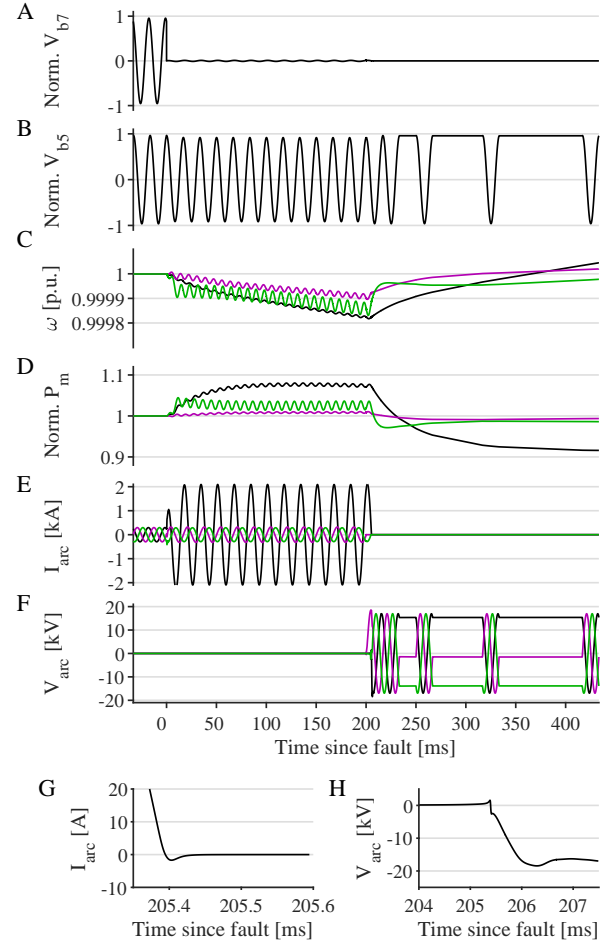


Figure 9. Detailed dynamics of the WSCC system immediately after the application of a single line-to-ground fault. (A-B) Phase A voltages at bus 7 of the feeder (A), where the fault is applied, and at bus 5 outside of the distribution feeder (B), normalized to their nominal values (12.47 and 230 kV, respectively). (C-D) Angular frequency and mechanical power of the 3 generators of the system (black, magenta and green traces, respectively). Each value of mechanical power is normalized to its baseline value before the application of the fault. (E) Arc current flowing through each phase of the SF6 circuit breaker. Notice how the increase in arc current is more marked in the phase on which the fault is applied (black trace) (F) Arc voltage across the three phases of the SF6 circuit breaker. (G-H) Enlargements of the arc current (G) and voltage (H) dynamics around the opening time of the breaker.

the obtained solution. Additionally, in the same simulation one can include models described at different levels of complexity to investigate specific dynamics of the system.

#### D. The modified IEEE 14-bus test system

The final test system we considered is a modified version of the well-known and largely used IEEE-14 power system, shown in Fig. 10: the distribution feeder used so far (Fig. 3) was connected to bus 4 and a solar plant (Fig. 11, top) was connected to bus 7 of the feeder. The solar plant generates 4.87 MW when irradiance is  $1 \text{ kW/m}^2$ . We added a 36 mHz dead-band to the turbine governor of the largest synchronous generator G1 [44]. The solar plant was connected to the feeder through the three-phase LCL filter-based voltage source converter (VSC) and the DC/DC converter shown in Fig. 11.

Table II  
RMSE BETWEEN CONVENTIONAL EMT INTEGRATION AND EFM FOR THE TRACES SHOWN IN FIG. 9

Variable	Before fault		After fault	
	RMSE	Range	RMSE	Range
Bus 7 voltage	4.8 V	33.7 kV	N/A	N/A
Bus 5 voltage	79 V	626.8 kV	98 V	631 kV
Arc current (phase A)	80 mA	590 A	1.3 $\mu\text{A}$	4.3 kA
Arc current (phase B)	44 mA	592 A	1.5 $\mu\text{A}$	638 A
Arc current (phase C)	37 mA	590 A	1.4 $\mu\text{A}$	696 A
Arc voltage (phase A)	7.5 mV	57 mV	5.6 V	35.6 kV
Arc voltage (phase B)	4.3 $\mu\text{V}$	58 mV	5.4 V	35.5 kV
Arc voltage (phase C)	3.6 $\mu\text{V}$	57 mV	5.6 V	34.2 kV

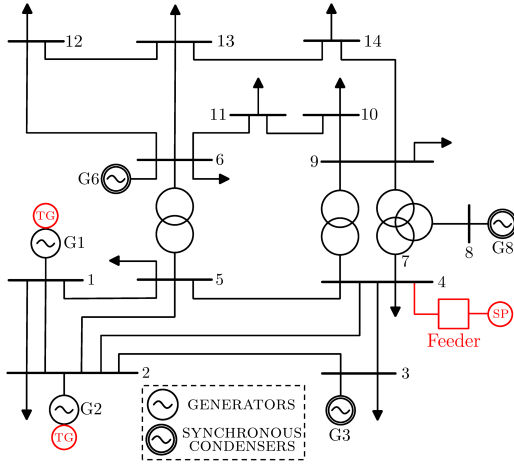


Figure 10. High-level block schematic of the modified IEEE-14 power system. The solar plant (labeled with  $\text{SP}$ ) is connected to the main network by means of the feeder shown in Fig. 3. Turbine governors installed in synchronous machines are labeled with  $\text{TG}$ .

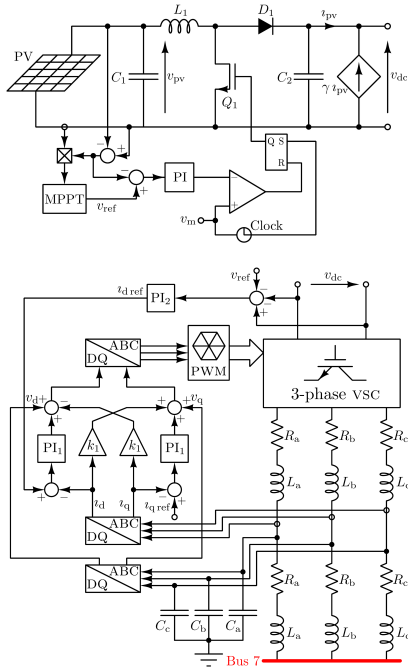


Figure 11. Schematics of the photovoltaic power plant (top) and of the voltage source converter (bottom) through which the power plant is connected to bus 7 of the feeder in the IEEE-14 network.

A detailed description of the solar plant and connectors can be found in [14]: briefly, the proportional-integral (PI) control block labeled  $\text{PI}_2$  senses the  $v_{\text{dc}}$  input voltage of the VSC and acts on the  $i_{\text{d,ref}}$  signal (d-axis reference current) so that  $v_{\text{dc}}$  is kept at  $v_{\text{ref}}$ . The DC-side of the VSC is connected to the DC/DC converter that transfers power from solar panels of the photovoltaic plant. The DC/DC converter is equipped with a perturb and observe (P&O) maximum power point tracker (MPPT) [45] (but see [46] for a potentially faster implementation of the P&O algorithm). The MPPT senses the instantaneous power delivered by the solar plant with a period

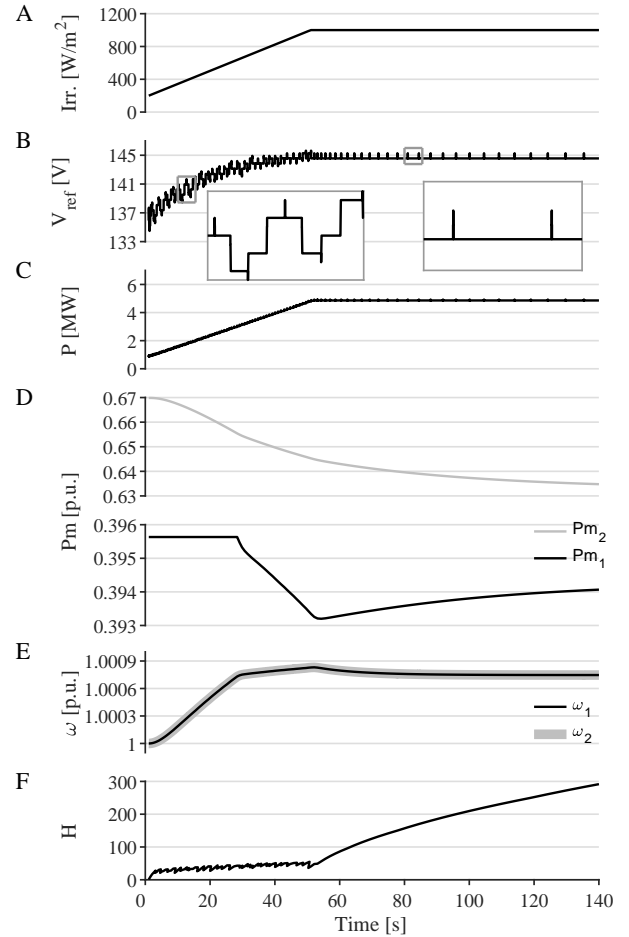


Figure 12. Dynamics of the IEEE-14 system following an increase in the irradiance of the photovoltaic plant connected to bus 7 of the feeder. (A) The irradiance increases linearly from 200 to 1000  $\text{W}/\text{m}^2$  over the course of 60 s. (B) Instantaneous voltage across the photovoltaic plant set by the P&O MPPT. Insets: zooms of the dynamics in the boxed regions of the main panel. Each “spike” corresponds to a detailed integration of one period (i.e.,  $T = 1/60$  s) of the system, required for the computation of the envelope vector field, as described in Eq. 3. (C) Electrical power injected by the photovoltaic plant at bus 7 of the feeder. (D) Mechanical power from the prime mover of generators G1 and G2 (black and gray traces respectively). (E) Rotor speeds of generators G1 and G2 (black and gray traces respectively). (F) Time steps taken by the EFM over the course of the simulation in units of  $T$  of the three-phase system.

of  $T/4$  (in our case  $T = 1/60$  s) and varies the  $v_{\text{ref}}$  reference voltage by a discrete step to obtain the maximum power generation from the photovoltaic array. The duty-cycle of the DC/DC converter is varied in order to set the  $v_{\text{pv}}$  voltage of the photovoltaic array required to meet the maximum power transfer condition.

Our target is to perform an electromagnetic transient analysis of the modified IEEE-14 hybrid power system when clouds clear the solar arrays and the irradiance  $S$  increases linearly from 200 to 1000  $\text{W}/\text{m}^2$  in about 60 s. Starting from the PF solution, a simulation lasting for 140 s was performed by using the proposed EFM approach. As shown in Fig. 12, while the irradiance  $S$  increases (panel A), so does the voltage across the photovoltaic plant due to the action of the MPPT (panel B). The periodic action performed by the MPPT lasts for one period  $T$

and appears as “spikes” in the voltage waveforms shown in the insets of Fig. 12B: consecutive spikes are separated by a time corresponding to the time steps of the EFM (shown in panel F), highlighting the efficiency increase with respect to conventional EMT analysis. As a consequence of the increase in irradiance, the power generated by the photovoltaic plant also increases (panel C) and this in turn causes a reduction of the mechanical power generated by the prime movers of the synchronous generators G1 and G2 (panel D, black and gray traces respectively) and a consequent increase in their rotor speeds (panel E, black and gray traces still relate to G1 and G2, respectively). Notice that  $P_{m1}$  remains constant as long as  $\omega_1$  remains within the amplitude of the dead-band: once  $\omega_1$  is outside the bounds determined by the dead-band, also G1 contributes to compensate frequency variations. From these results we can see that, even if  $S$  reaches its maximum level after about 60 s, requiring  $60 \times 4 \times 60 = 14400$  cycles of the MPPT, the system frequency stabilizes after about 120 s. Finally, Fig. 12F shows the time steps  $H$  taken by the EFM during simulation: during the transient part of the simulation, i.e., before  $S$  reaches a steady-state value,  $H$  is between  $25T$  and  $50T$ . Conversely, once  $S$  has reached its maximum value, the system stabilizes and  $H$  progressively increases to higher values (around  $250 - 300T$ ), indicating a substantial increase in simulation efficiency. This is confirmed by the fact that the actual simulation times were 11512 s and 461 s for the conventional and envelope-following algorithms, respectively, corresponding to an approximately  $25 \times$  speed-up. At the same time, the RMSE for the traces shown in Fig. 12 (reported in Table III) is approximately two orders of magnitude smaller than the range of variability of each variable, indicating a good match between conventional and EFM solutions.

Once again, we stress the fact that these results have been obtained by modeling the IEEE-14 bus test system with the dynamic single-phase equivalent model while the feeder, converters, MPPT and photovoltaic plant are described by a detailed (three-phase) dynamic model.

## V. DISCUSSION AND CONCLUDING REMARKS

In this paper we have shown how to apply the envelope-following technique to the simulation of hybrid power systems, made up of several types of energy sources connected with conventional and non-conventional loads by means of HVDC and MTDC systems. The main novelty of our work lies in the fact that, unlike other commonly used simulation approaches [2], [3], [7], [8], we use a single simulation engine for both the EMT and phasor domain parts of the system.

Table III  
RMSE BETWEEN CONVENTIONAL EMT INTEGRATION AND EFM FOR THE TRACES SHOWN IN FIG. 12

Variable	RMSE	Range
MPPT voltage	0.7 V	11.2 V
MPPT power	20.1 kW	40.4 MW
Generator 1 power	4.3 m p.u.	45 $\mu$ p.u.
Generator 2 power	37.2 m p.u.	0.1 m p.u.
Generator 1 angular frequency	0.88 m p.u.	6 $\mu$ p.u.
Generator 2 angular frequency	0.88 m p.u.	6 $\mu$ p.u.

We achieve this by using so-called virtual connectors [13], which, at the minor cost of discarding the zero sequence, allow eliminating the need for the complex control strategies required to synchronize two concurrently running simulators. In particular, no information regarding the zero-sequence is lost if unbalances are confined (by transformers) only in the ESS portion of the power system and virtual connectors are placed next to  $\Delta Yg$  transformers (with the wye and delta windings connected respectively to the electromagnetic and power sub-systems). Besides, since  $\Delta Yg$  transformers have an infinite zero-sequence impedance, no zero-sequence current can flow from the wye to the delta windings. The same holds if the transformer adopted is of  $YYg$  type.

We validated our method by presenting three test cases of increasing complexity: in the first one we highlighted the general features of the EFM and its capability of automatically handling discontinuities, such as faults, in the simulation. The second one concerned the WSCC 9-bus system and showed how one can easily incorporate increasing levels of detail in the models of the components employed in the 3-phase part of the simulation, and finally, with the third test case, a modified version of the IEEE-14 power system, we showed how the EFM is suitable for application to systems containing inverter-based resources. Performance comparisons with a conventional, variable time step transient analysis shows that the speed-up attributable to the EFM ranges from one to two orders of magnitude, while at the same time not requiring the cumbersome heuristics employed by simulators such as those described in [2], [3].

Finally, given the widespread penetration of electronics in modern-day power systems, the usage of a single electrical and power circuit simulator allows incorporating into the same simulation all the detailed models of electronic components that have been developed over the years.

## APPENDIX

To support the reader in fully grasping the structure of Eq. 2 and further demonstrate that the envelope-following method (EFM) can be used to simulate AC/DC systems, we consider the basic case-study shown in Fig. 13. This system comprises a simplified model of an AC electro-mechanical system (synchronous generator  $G$ ) connected by a DC/AC converter (controlled sources) to a HVDC link ( $R_{dc}$ ). The other side of the HVDC link is connected to an infinite DC bus, which imposes the voltage  $V_{dc}$  regardless of grid

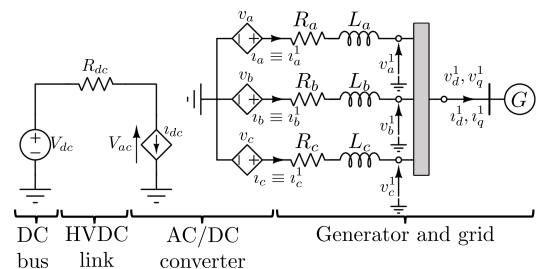


Figure 13. Simplified AC/DC system.

operating conditions. Being sufficiently simple, on the whole, the dynamical evolution of this AC/DC system is governed by the following set of DAEs

$$\dot{\delta} = \Omega(\omega - 1) \quad (8a)$$

$$M\dot{\omega} = P_m - (v_d^1 v_d^1 + v_q^1 v_q^1) - D(\omega - 1) \quad (8b)$$

$$L_k \dot{i}_k^1 = v_k - R_k i_k^1 - v_k^1 \quad (8c,d,e)$$

$$v_d^1 = E_g \cos(\delta) \quad (8f)$$

$$v_q^1 = E_g \sin(\delta) \quad (8g)$$

$$v_a = V_{ac} \sin(\Omega t + \varphi) \quad (8h)$$

$$v_b = V_{ac} \sin(\Omega t + \varphi + 2\pi/3) \quad (8i)$$

$$v_c = V_{ac} \sin(\Omega t + \varphi + 4\pi/3) \quad (8j)$$

$$\frac{V_{ac}(V_{dc} - V_{ac})}{R_{dc}} = (v_a i_a^1 + v_b i_b^1 + v_c i_c^1) \quad (8k)$$

$$\mathbf{v}_{a,b,c}^1 = \Xi^T \mathbf{v}_{d,q}^1 \quad (8l)$$

$$\mathbf{i}_{d,q}^1 = \Xi \mathbf{i}_{a,b,c}^1, \quad (8m)$$

where  $k \in \{a, b, c\}$ . Eqs. 8a-e are differential and the remaining ones are algebraic. Eqs. 8a-b and f-g describe the type-II model  $G$  synchronous generator. The voltage-controlled current source at the DC side and the voltage-controlled voltage-sources at the AC side (see Fig. 13) are related by Eqs. 8h-k, where  $\Omega = 2\pi \times 50$  Hz is the synchronous frequency of the power system, while the variables  $V_{ac}$  and  $\varphi$  can be controlled to attain a given active and reactive power exchange. These controlled sources implement an ideal power transfer between the DC and AC sides of the converter (i.e., no internal losses). The virtual connector between the three-phase sub-systems and the single phase one (see the gray box in Fig. 13) implements the ABC-DQ transformation (through matrix  $\Xi$ ) from the  $\mathbf{v}_{a,b,c}^1$  to the  $\mathbf{v}_{d,q}^1$  currents and the DQ-ABC transformation (through matrix  $\Xi^T$ ) from the  $\mathbf{v}_{d,q}^1$  to the  $\mathbf{v}_{a,b,c}^1$  voltages (see Eqs. 8l-m). In this simple example, the state variables on the three-phase side coincide with the  $\mathbf{v}_{d,q}^1$  virtual-connector currents.

It is straightforward to properly collect the equations of Eq. 8 and organize them to obtain the generic compact representation given in Eq. 2. In particular,  $\xi = (\delta, \omega, v_a^1, v_b^1, v_c^1)^T$  and  $\psi = (v_d^1, v_q^1, i_d^1, i_q^1, v_a, v_b, v_c, v_a^1, v_b^1, v_c^1, V_{ac})^T$ .

We simulated this simple system as follows: first, we used the method in [13] to compute its periodic steady state solution, which is periodic in the three-phase subsystem and constant in the DC and single-phase ones. We then performed an EFM analysis by varying  $\varphi$  in Eqs. 8h-k from 0 to 10° after 10 s from the start of the time domain analysis. This variation emulates a permanent phase shifting of a phase locked loop (PLL) (which would be present in the real control scheme of an AC/DC converter). Figure 14 reports some results obtained with the conventional transient stability analysis and the EFM, which took 98 s and 260 ms to complete, respectively.

## REFERENCES

[1] S. S. Martin, A. Chebak, A. El Ouafi, and M. Mabrouki, "Modeling and simulation of hybrid power system integrating wind, solar, biodiesel energies and storage battery," in *2016 International Renewable and Sustainable Energy Conference (IRSEC)*, pp. 457–463, 2016.

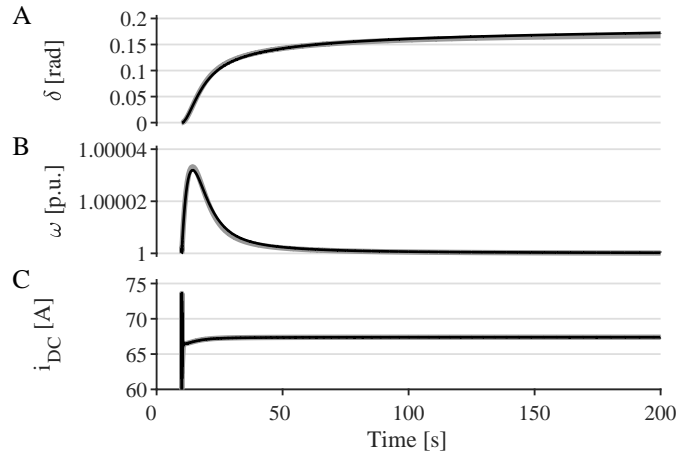


Figure 14. Dynamics of a simplified AC/DC system computed with a conventional integration algorithm and with the EFM. (A,B) Rotor angle and angular speed of the synchronous generator  $G$ . (C) The  $i_{dc}$  current shown in Fig. 13. All traces almost perfectly overlap.

[2] Q. Huang and V. Vittal, "Integrated transmission and distribution system power flow and dynamic simulation using mixed three-sequence/three-phase modeling," *IEEE Transactions on Power Systems*, vol. 32, no. 5, pp. 3704–3714, 2017.

[3] Q. Huang and V. Vittal, "Advanced EMT and phasor-domain hybrid simulation with simulation mode switching capability for transmission and distribution systems," *IEEE Transactions on Power Systems*, vol. 33, no. 6, pp. 6298–6308, 2018.

[4] E. Zhijun, D. Fang, K. Chan, and S. Yuan, "Hybrid simulation of power systems with SVC dynamic phasor model," *International Journal of Electrical Power & Energy Systems*, vol. 31, no. 5, pp. 175–180, 2009.

[5] D. Fang, W. Liwei, T. Chung, and K. Wong, "New techniques for enhancing accuracy of EMTP/TSP hybrid simulation," *International Journal of Electrical Power & Energy Systems*, vol. 28, no. 10, pp. 707–711, 2006.

[6] Q. Huang, R. Huang, B. J. Palmer, Y. Liu, S. Jin, R. Diao, Y. Chen, and Y. Zhang, "A reference implementation of WECC composite load model in Matlab and GridPACK," *arXiv preprint arXiv:1708.00939*, 2017.

[7] S. Zhang, Y. Zhu, K. Ou, Q. Guo, Y. Hu, and W. Li, "A practical real-time hybrid simulator for modern large HVAC/DC power systems interfacing RTDS and external transient program," in *2016 IEEE Power and Energy Society General Meeting (PESGM)*, pp. 1–5, IEEE, 2016.

[8] A. Hariri and M. O. Faruque, "A hybrid simulation tool for the study of PV integration impacts on distribution networks," *IEEE Transactions on Sustainable Energy*, vol. 8, no. 2, pp. 648–657, 2016.

[9] Q. Huang and V. Vittal, "Application of electromagnetic transient-transient stability hybrid simulation to FIDVR study," *IEEE Transactions on Power Systems*, vol. 31, no. 4, pp. 2634–2646, 2015.

[10] A. A. van der Meer, M. Gibescu, M. A. van der Meijden, W. L. Kling, and J. A. Ferreira, "Advanced hybrid transient stability and EMT simulation for VSC-HVDC systems," *IEEE Transactions on Power Delivery*, vol. 30, no. 3, pp. 1057–1066, 2014.

[11] F. J. Plumier, P. Aristidou, C. Geuzaine, and T. Van Cutsem, "A relaxation scheme to combine phasor-mode and electromagnetic transients simulations," in *2014 Power Systems Computation Conference*, pp. 1–7, IEEE, 2014.

[12] X. Lin, A. Gole, and M. Yu, "A wide-band multi-port system equivalent for real-time digital power system simulators," *IEEE Transactions on Power Systems*, vol. 24, no. 1, pp. 237–249, 2008.

[13] F. Bizzarri and A. Brambilla, "Generalized power flow analysis of electrical power systems modeled as mixed single-phase/three-phase sub-systems," *IEEE Transactions on Power Systems*, vol. 35, no. 2, pp. 1284–1293, 2019.

[14] F. Bizzarri, D. del Giudice, D. Linaro, and A. Brambilla, "Numerical approach to compute the power flow solution of hybrid generation, transmission and distribution systems," *IEEE Transactions on Circuits and Systems II: Express Briefs*, vol. 67, no. 5, pp. 936–940, 2020.

[15] D. Linaro, D. del Giudice, A. Brambilla, and F. Bizzarri, "Application

- of envelope-following techniques to the shooting method," *IEEE Open Journal of Circuits and Systems*, vol. 1, pp. 22–33, 2020.
- [16] Y. Wang, P. Li, and S. Lai, "Robust and efficient transistor-level envelope-following analysis of PWM/PFM/PSM DC-DC converters," *IEEE Transactions on Computer-Aided Design of Integrated Circuits and Systems*, vol. 35, no. 11, pp. 1836–1847, 2016.
- [17] A. Brambilla and P. Maffezzoni, "Envelope-following method to compute steady-state solutions of electrical circuits," *IEEE Transactions on Circuits and Systems I: Fundamental Theory and Applications*, vol. 50, no. 3, pp. 407–417, 2003.
- [18] L. R. Petzold, L. O. Jay, and J. Yen, "Numerical solution of highly oscillatory ordinary differential equations," *Acta Numerica*, vol. 6, p. 437–483, 1997.
- [19] L. R. Petzold, "An efficient numerical method for highly oscillatory ordinary differential equations," *SIAM Journal on Numerical Analysis*, vol. 18, no. 3, pp. 455–479, 1981.
- [20] P. Kundur, N. Balu, and M. Lauby, *Power system stability and control*. EPRI power system engineering series, McGraw-Hill, 1994.
- [21] I. Kocar, J. Mahseredjian, U. Karaagac, G. Soykan, and O. Saad, "Multiphase load-flow solution for large-scale distribution systems using MANA," *IEEE Trans. on Power Delivery*, vol. 29, pp. 908–915, April 2014.
- [22] C.-W. Ho, A. Ruehli, and P. Brennan, "The modified nodal approach to network analysis," *IEEE Transactions on circuits and systems*, vol. 22, no. 6, pp. 504–509, 1975.
- [23] F. Bizzarri, A. Brambilla, and F. Milano, "The probe-insertion technique for the detection of limit cycles in power systems," *IEEE Transactions on Circuits and Systems I: Regular Papers*, vol. 63, no. 2, pp. 312–321, 2016.
- [24] U. M. Ascher and L. R. Petzold, *Computer methods for ordinary differential equations and differential-algebraic equations*, vol. 61. Siam, 1998.
- [25] M. A. M. Shaheen, H. M. Hasanien, S. F. Mekhamer, and H. E. A. Talaat, "Optimal power flow of power systems including distributed generation units using sunflower optimization algorithm," *IEEE Access*, vol. 7, pp. 109289–109300, 2019.
- [26] A. Trias and J. L. Marín, "The holomorphic embedding loadflow method for DC power systems and nonlinear DC circuits," *IEEE Transactions on Circuits and Systems I: Regular Papers*, vol. 63, no. 2, pp. 322–333, 2016.
- [27] M. A. Farhan, M. S. Nakhla, E. Gad, and R. Achar, "Parallel high-order envelope-following method for fast transient analysis of highly oscillatory circuits," *IEEE Transactions on Very Large Scale Integration (VLSI) Systems*, vol. 25, no. 1, pp. 261–270, 2016.
- [28] M. A. Farhan, E. Gad, M. S. Nakhla, and R. Achar, "High order and a-stable envelope following method for transient simulations of oscillatory circuits," *IEEE Transactions on Microwave Theory and Techniques*, vol. 62, no. 12, pp. 3309–3317, 2014.
- [29] S. Sancho, A. Suarez, and J. Chuan, "General envelope-transient formulation of phase-locked loops using three time scales," *IEEE Transactions on Microwave Theory and Techniques*, vol. 52, pp. 1310–1320, April 2004.
- [30] K. Kundert, J. White, and A. Sangiovanni-Vincentelli, "An envelope-following method for the efficient simulation of switching power and filter circuits," in *[1988] IEEE International Conference on Computer-Aided Design (ICCAD-89) Digest of Technical Papers*, pp. 446–449, Nov 1988.
- [31] C. W. Gear, *Numerical Initial Value Problems in Ordinary Differential Equations*. Prentice-Hall, 1971.
- [32] F. Bizzarri, A. Brambilla, G. S. Gajani, and S. Banerjee, "Simulation of real world circuits: Extending conventional analysis methods to circuits described by heterogeneous languages," *IEEE Circuits and Systems Magazine*, vol. 14, pp. 51–70, Fourthquarter 2014.
- [33] F. Bizzarri and A. Brambilla, "PAN and MPanSuite: Simulation vehicles towards the analysis and design of heterogeneous mixed electrical systems," in *2017 New Generation of CAS (NGCAS)*, pp. 1–4, IEEE, 2017.
- [34] IEEE PES AMPS DSAS Test Feeder Working Group, "Distribution test feeders," 2010.
- [35] K. Schneider, B. Mather, B. Pal, C.-W. Ten, G. Shirek, H. Zhu, J. Fuller, J. Pereira, L. Ochoa, L. De Araujo, *et al.*, "Analytic considerations and design basis for the IEEE distribution test feeders," *IEEE Transactions on power systems*, vol. 33, no. 3, pp. 3181–3188, 2017.
- [36] A. AL-Hinai, "WSCC 9-bus system," 2000.
- [37] D. Asija, P. Choudekar, K. Soni, and S. Sinha, "Power flow study and contingency status of WSCC 9 Bus test system using MATLAB," in *2015 International Conference on Recent Developments in Control, Automation and Power Engineering (RDCAPE)*, pp. 338–342, IEEE, 2015.
- [38] R. Terzioğlu and T. F. Çavuş, "Probabilistic load flow analysis of the 9 bus WSCC system," *International Journal of Scientific and Research Publications*, vol. 3, no. 9, 2013.
- [39] K. Meah and A. S. Ula, "Simulation study of the CIGRE HVDC benchmark model with the WSCC nine-bus power system network," in *2009 IEEE/PES Power Systems Conference and Exposition*, pp. 1–5, IEEE, 2009.
- [40] F. Bizzarri and A. Brambilla, "Brushing up on the Urbanek black box arc model," *IEEE Transactions on Circuits and Systems I: Regular Papers*, vol. 65, no. 5, pp. 1675–1683, 2018.
- [41] S. Leung, L. A. Snider, and C. S. Wong, "SF6 generator circuit breaker modeling," in *International Conference on Power Systems Transients (IPST'05), Montreal, Canada*, pp. 19–23, 2005.
- [42] A. Lee, P. Slade, K. Yoon, J. Porter, and J. Vithayathil, "The development of a HVDC SF6 breaker," *IEEE transactions on power apparatus and systems*, no. 10, pp. 2721–2729, 1985.
- [43] F. Bizzarri, G. Gruosso, M. Bonaconsa, and A. Brambilla, "A reliable and efficient black box model of SF6 medium voltage circuit breakers," *International Journal of Electrical Power and Energy Systems*, vol. 119, 2020.
- [44] North American Electric Reliability Corporation (NERC), *Balancing and Frequency Control*, 2011.
- [45] A. Brambilla, M. Gambarara, and G. Torrente, "Perturb and observe digital maximum power point tracker for satellite applications," in *Proc. of the Sixth European Conference, ESA, (Porto, Portugal)*, pp. 263–267, European Space Agency, May 2002.
- [46] V. Saxena, N. Kumar, B. Singh, and B. K. Panigrahi, "A rapid circle centre-line concept-based MPPT algorithm for solar photovoltaic energy conversion systems," *IEEE Transactions on Circuits and Systems I: Regular Papers*, vol. 68, no. 2, pp. 940–949, 2021.



realistic single-cell models of neuronal cells.

**Daniele Linaro** received his MSc in Electronic Engineering from the University of Genoa (Italy) in 2007 and a PhD in Electrical Engineering from the same university in 2011. Since 2018, he is Assistant Professor in the Department of Electronics, Information Technology and Bioengineering at the Polytechnic of Milan. His main research interests are currently in the area of circuit theory and nonlinear dynamical systems, with applications to electronic oscillators and power systems and computational neuroscience, in particular biophysically-



**Davide del Giudice** was born in Milan, Italy, in July 1993. He received the B.S. degree and the M.S. degree (cum laude) in electrical engineering from Politecnico di Milano, Italy in 2015 and 2017 respectively. He is currently a PhD candidate at the department of Electronics, Information and Bioengineering of the Politecnico di Milano. His main research activities are related to simulation techniques specifically tailored to electric power systems characterised by a high penetration of renewable energy sources, such as HVDC systems.



**Angelo Brambilla** (M'16) received the Dr. Ing. degree in electronics engineering from the University of Pavia, Pavia, Italy, in 1986. He is full professor at the Dipartimento di Elettronica, Informazione e Bioingegneria, Politecnico di Milano, Milano, Italy, where he has been working in the areas of circuit analysis, simulation and modeling.



**Federico Bizzarri** (M'12–SM'14) was born in Genoa, Italy, in 1974. He received the Laurea (M.Sc.) five-year degree (*summa cum laude*) in electronic engineering and the Ph.D. degree in electrical engineering from the University of Genoa, Genoa, Italy, in 1998 and 2001, respectively. Since October 2018 he has been an associate professor at the Electronic and Information Department of the Politecnico di Milano, Milan, Italy. He is a research fellow of the Advanced Research Center on Electronic Systems for Information and Communication Technologies

“E. De Castro” (ARCES), University of Bologna, Italy. He served as an Associate Editor of the IEEE Transactions on Circuits and Systems — Part I from 2012 to 2015 and he was awarded as one of the 2012-2013 Best Associate Editors of this journal.